Powder Technology 266 (2014) 22–37

Contents lists available at ScienceDirect

Powder Technology

journal homepage: www.elsevier.com/locate/powtec

Numerical analysis of particle flows within a double expansion

A.I.J. Love *, D. Giddings, H. Power

Division of Energy and Sustainability, The University of Nottingham, University Park, Nottingham, NG7 2RD, United Kingdom

ARTICLE INFO

Article history:
Received 3 September 2013
Received in revised form 28 May 2014
Accepted 31 May 2014
Available online 11 June 2014

Keywords:
Computational fluid dynamics
Two-phase flow
Pulverised fuel
Coanda effect

ABSTRACT

The effect of solid particles within flows having zones of recirculation is of interest in pulverised fuel distribution and combustion at burners. Previous modelling of a 1/4 scale test rig was performed by Giddings et al. (2004), and an instability was later identified within the domain. Subsequently the transient dynamics of the flow of air through a double expansion were investigated numerically and a recirculation zone was found to develop at one of the four corners of the expansion. In the work presented here the flow of solid particles through this double expansion is investigated using the commercial software ANSYS FLUENT R14.0. The Stress-Omega Reynolds Stress Model is used to model the gas phase turbulence and the Discrete Particle Model is used to model the solid particle flow. The dynamics of the flow are reported here for 10 μm and 60 μm particles and for mass loadings from 0 to 1 $kg_{particles}/kg_{air}$. The simulations show a distinct transition to a vortex shedding type instability with the addition of the discrete phase. Furthermore, for increasing mass loading and particle Stokes number the Coanda effect is reduced leading to two large recirculation zones in opposing corners of the domain. The characteristics of the flow field are in qualitative agreement with studies of particle flows in jet flows and shear layers. This work serves to highlight some of the challenges in modelling complex pneumatic conveying flows from an industrial perspective.

1. Introduction

The steady pneumatic transport of solid particles is of importance to many industries. This is particularly true of coal fired power plants where coal is first ground in the mills before being pneumatically transported to a number of burners through a convoluted system of pipes and splitters. In order to ensure good performance a steady homogeneous supply of fuel to the burners is desirable. The presence of flow features, such as a recirculation zone at expansions, further complicates the picture. For example, the study by Kuan and Yang [1] highlighted the unsteady flow downstream of a bifurcation. In addition, the interaction of pulverised fuel with a recirculation is key to the stability and NO_x performance of low NO_x burners. Computational fluid dynamics is utilised within industry to model such flows where simplifications, such as steady state analysis, are common but may not result in numerically stable solutions. In this study the flow through a double expansion is investigated and the effect of the discrete phase on the flow is evaluated.

There are a number of examples in the literature of flow through circular-to-rectangular transition ducts [2–4]. Patrick and McCormick [2] found asymmetric flow within a circular-to-rectangular transition duct. Miau et al. [3] went on to investigate the flow field in three transition ducts of constant cross sectional area, but different lengths, over a range of turbulent Reynolds numbers. A separation bubble, or stall region, was found in one corner for the lowest Reynolds number case, disappearing at higher Reynolds numbers. Characteristics of the flow depended primarily on the geometry. However, diffuser geometries do not maintain a constant cross sectional area but expand in two or three dimensions. Therefore, a greater adverse pressure gradient is present and boundary layer separation is more likely. Turbulent flow through two dimensional diffusers can generate a number of flow regimes: attached flow to both divergent walls, unsteady transitory stall, fully developed large stall/recirculation region, a hysteresis region and jet flow regime [5]. The transitory stall regime is characterised by the formation of a large recirculation in one corner.

The flows over backward facing steps, through diffusers and around bluff bodies are subject to a number of flow phenomena including separation, the Coanda effect, jet precession and vortex shedding. The Coanda effect is the deflection of a jet due to the generation of a low pressure region next to the jet as it entrains fluid [6], and precession being the rotation of a jet around an axis [7]. Reynolds Averaged Navier Stokes (RANS) turbulence models have been shown to capture the main flow features in each case. For example, the separation bubble in 2D and 3D diffusers has been captured by Reynolds Stress Models (RSMs) [8–10], Guo et al. [7] reproduced jet precession in an axisymmetric expansion, whilst Lardeau and Leschziner [11] and Iaccarino et al. [12] captured vortex shedding behind bluff bodies. Large Eddy Simulation (LES) models the smallest turbulent scales using sub-grid scale models

* Corresponding author.
E-mail addresses: enxail@nottingham.ac.uk (A.I.J. Love), donald.giddings@nottingham.ac.uk (D. Giddings), henry.power@nottingham.ac.uk (H. Power).

http://dx.doi.org/10.1016/j.powtec.2014.05.057

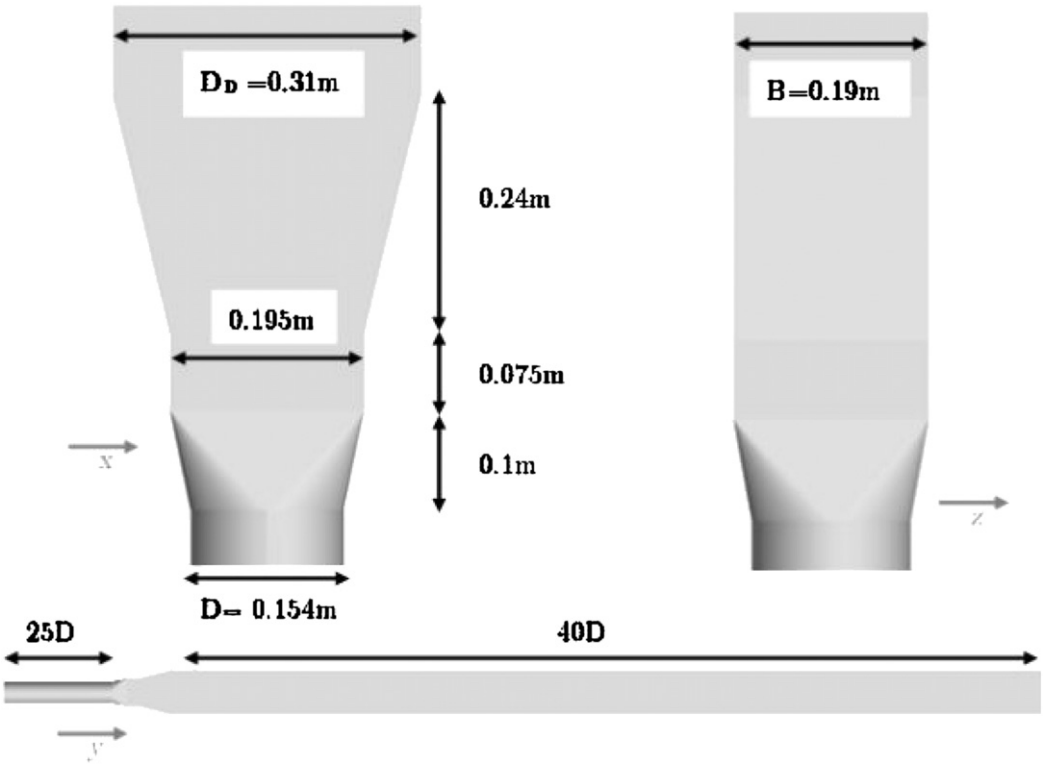

Fig. 1. Dimensions of the diffuser geometry.

and is capable of capturing both the random fluctuations in the fluid velocity and the largest turbulence structures. This approach has been utilised with good results for diffuser and bluff body flows [13,14]. Despite this LES still represents considerable computational expense in comparison to RANS models for industrially relevant confined flows at high Reynolds number [15]. By formulation RANS models average out the random velocity fluctuations, modelling the transport of turbulent kinetic energy and its dissipation, but have been found to capture the largest, deterministic scales of turbulence such as vortex shedding [12,11]. Furthermore, Garnier et al. [10] showed that unsteady RANS was capable of reproducing the reduction in the re-attachment length for a separated flow by periodic forcing at the optimum frequency. Although URANS underpredicted the reduction in recirculation length compared to LES especially at high forcing frequency as URANS filters the smallest turbulent fluctuations, from a practical point of view the prediction of the separation bubble and forcing response was found to be adequate.

The characteristics of particles and their impact on such complex flows have been investigated both experimentally and numerically. The dispersion of particles at a recirculation downstream of a backward facing step was investigated experimentally by Hardalupas [16]. Particles only enter the recirculation zone due to turbulent dispersion as they must cross the dividing streamline. They found bimodal probability distribution functions for both axial and inclined velocities near the shear layer for a large eddy Stokes number of 1. Particle concentration in the recirculation zone increased abruptly for a Stokes number of 1. Eaton and Fessler [17] provide an overview of preferential particle concentration by turbulence. It has been shown for many flows that small particles concentrate on the outside and between coherent vortex structures. Horender and Hardalupas [18] used PIV to gather measurements in a horizontal plane shear layer laden with mono-dispersed glass particles of sizes 55 and 90 μm. The experimental results showed that large eddies centrifuged particles into the low speed side of the flow, contributing to large particle velocity fluctuations. In addition, bimodal

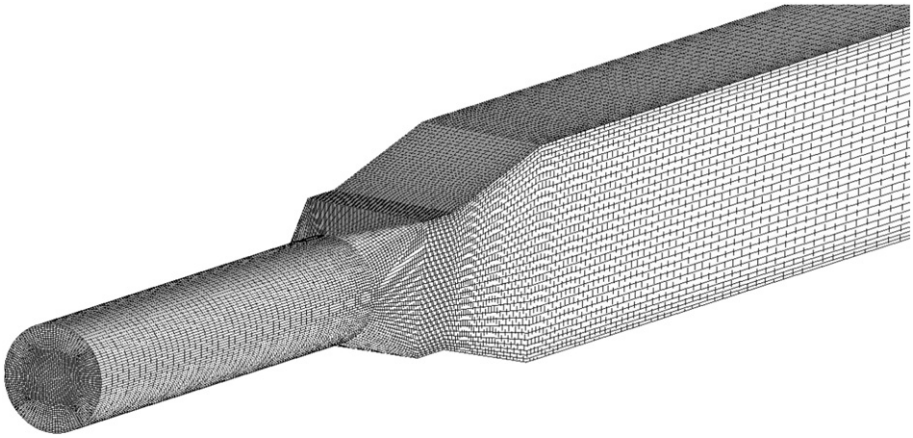

Fig. 2. Example of computational grid.

particle concentration distributions were observed due to coherent vortex structures.

Meiburg et al. [19] modelled the fluid vorticity field for particle laden mixing layers using a Eulerian–Lagrangian approach including two-way coupling. For the case of differential particle loading between two streams a direct shift was observed in the Kelvin–Helmholtz vortex towards the seeded stream compared to the uniform particle distribution case. This was due to an increase in vorticity generation on the side of the seeded stream. Founti and Klipfel [20] investigated the effects of particle collisions on the flow past a sudden expansion using a closed loop diesel oil circuit and computational modelling. They found that the particle concentration increased in the shear layer due to inter-particle collisions, compared to the recirculation zone and core jet flow. In addition, they saw a decrease in reattachment length for low mass loadings which was attributed to higher particle fluctuations in the recirculation zone. The reduction in the particle fluctuations was due to inter-particle collisions which lead to a subsequent increase in recirculation zone length. Based on the modelling results the inclusion of the particle collision makes a small contribution to the profiles of particle turbulent kinetic energy.

The modelling of confined particle flows has focused on characterising the particle phase. Steady state modelling approaches have been used to capture the particle concentration profiles and particle velocities within different pipe geometries [21–23]. The interaction of particles with recirculation zones is of most relevance to the design of multiphase burners. The bluff body flow of Borée et al. [24] has subsequently been used to validate and compare the performance of LES and unsteady RANS approaches [15,25]. It was shown that even for the low mass loading case, two-way coupling effects had a significant impact on the continuous flow field close to the main axis of the flow. An unsteady RANS approach using the k-ϵ turbulence model was found to be in good agreement with the flow characteristics [15]. LES was used to investigate the effect of mass loading where the additional momentum of the high mass loading case strongly influenced the radial velocity fluctuations close to the access and the radial dispersion of the particles [25].

Previous modelling of a 1/4 scale test rig, resembling a section of a pulverised fuel piping system, was performed [22]. An instability was later identified within the domain. Within the geometry of the bifurcator a recirculation zone became established and it was observed that the interaction of the particle phase with this recirculation zone made a satisfactory steady state solution impossible. Subsequently the transient dynamics of the flow through a double expansion have been investigated numerically and a recirculation zone was found to develop at one of the four corners of the expansion, together with evidence of a precessing motion of the jet [26]. The present study examines the effects of the particles on this flow field. The commercial CFD code ANSYS FLUENT R14.0 is used. The dynamics of the flow are investigated for 10 μm and 60 μm particles over a range of mass loadings from 0.07 to 1 $kg_{particles}/kg_{air}$ and qualitatively compared to experimental and modelling work in the literature.

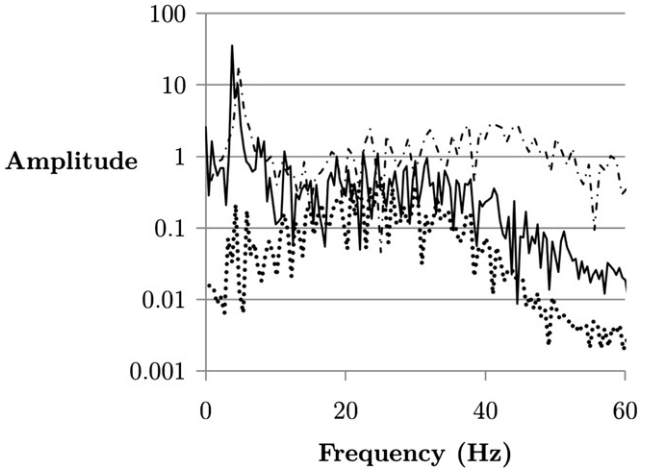

Fig. 3. Resultant secondary velocity oscillating frequencies 5D from the diffuser inlet on the [···] coarse mesh of 300,000 cells, [–.–] standard mesh of 600,000 cells subsequently used in this study and [– – –] refined mesh of 1,200,000 cells.

2. Model description

2.1. Geometry model and mesh

The modelled geometry was originally adapted from a bifurcator [22]. For the case of a straight inlet, attached to this geometry, a recirculation zone developed in each of the four corners, but larger recirculation zones formed in two opposing corners of the four. The two large recirculation zones were thought to be an outlet condition effect and so the flow has been studied with the bifurcator outlets removed. This resulted in the diffuser geometry with two expansions in series. Dimensions of the geometry are shown in Fig. 1.

A three dimensional structured grid was generated using ANSYS ICEM 13.0 (Fig. 2), with an O-grid used throughout and care taken to ensure orthogonality and a smooth variation of the cell structure across the domain. The cell density along the axis is non-uniform with

Table 1
Mass and momentum balance as well as RSM Stress-Omega equations. For further details see [28] and literature cited therein.

$$\frac{\partial \rho}{\partial t} + \nabla.\left(\rho \overrightarrow{u}\right) = 0 \tag{4.1}$$

$$\frac{\partial}{\partial t}\left(\rho \overrightarrow{u}\right) + \nabla.\left(\rho \overrightarrow{u}\,\overrightarrow{u}\right) = -\nabla p + \nabla.\left(\overline{\overline{\tau}}\right) + \rho \overrightarrow{g} \tag{4.2}$$

$$\begin{aligned}&\frac{\partial}{\partial t}\left(\rho\overline{u_i'u_j'}\right) + \frac{\partial}{\partial x_k}\left(pu_k\rho\overline{u_i'u_j'}\right) = -D_{T,ij} + \phi_{ij} + \frac{\partial}{\partial x_k}\left[\mu\frac{\partial}{\partial x_k}\left(\overline{u_i'u_j'}\right)\right]\\ &-\rho\left(\overline{u_i'u_k'}\frac{\partial u_j}{\partial x_k} + \overline{u_j'u_k'}\frac{\partial u_i}{\partial x_k}\right) - \epsilon_{ij} - 2\rho\Omega_k\left(\overline{u_j'u_m'}\epsilon_{ikm} + \overline{u_i'u_m'}\epsilon_{jkm}\right)\end{aligned} \tag{4.3}$$

$$D_{T,ij} = \frac{\partial}{\partial x_k}\left(\frac{\mu_t}{\sigma_k}\partial\frac{\overline{u_i'u_j'}}{\partial x_k}\right) \tag{4.4}$$

$$\begin{aligned}\phi_{ij} = &-C_1\rho\beta^*_{RSM}\omega\left[\overline{u_i'u_j'} - \frac{2}{3}\delta_{ij}k\right] - a_0\left[P_{ij} - \frac{1}{3}P_{kk}\delta_{ij}\right]\\ &-\widehat{\beta_0}\left[D_{ij} - \frac{1}{3}P_{kk}\delta_{ij}\right] - k\widehat{\gamma_0}\left[S_{ij} - \frac{1}{3}S_{kk}\delta_{ij}\right]\end{aligned} \tag{4.5}$$

$$D_{ij} = -\rho\left[\overline{u_i'u_m'}\frac{\partial u_m}{\partial x_j} + \overline{u_j'u_m'}\frac{\partial u_m}{\partial x_i}\right] \tag{4.6}$$

$$S_{ij} = \frac{1}{2}\left(\frac{\partial u_j}{\partial x_j} + \frac{\partial u_i}{\partial x_j}\right) \tag{4.7}$$

$$\epsilon_{ij} = \frac{2}{3}\sigma_{ij}\left(\rho\epsilon + 2\rho\epsilon\sqrt{\frac{k}{a^2}}\right) \tag{4.8}$$

Constants:

$$\widehat{a_0} = \frac{8 + C_2}{11}, \quad \hat{\beta}_0 = \frac{8C_2 - 2}{11}, \quad \widehat{\gamma_0} = \frac{60C_2 - 4}{55} \tag{4.9}$$

$$C_1 = 1.8, \quad C_2 = 0.52, \quad \sigma_k = 0.82 \tag{4.10}$$

neighbouring cells varying in size by no more than 10%. Fig. 3 shows the variation in the oscillating frequency of resultant secondary velocity 5D downstream of the diffuser entrance for the air flow only case. A mesh of 600,000 cells picked up distinct frequencies for the oscillating velocity fields for the $Re = 170,000$ air flow case. The mesh was refined to 1,200,000 cells which yielded a similar result for the main oscillating frequency. Peaks for both these cases are observed at 4.6 Hz, showing that the main low frequency oscillations are picked up by the mesh. On a coarser mesh (300,000 cells), the magnitude of all oscillations was reduced, and no distinct frequencies were visible. The length of the recirculation zone was consistent between each mesh being 1.16 m, 1.2 m and 1.18 m for the 300,000, 600,000 and 1,200,000 meshes respectively. The 600,000 cell mesh has been taken forward for the analysis in this study. At the diffuser this mesh featured cell lengths from 3.5 mm at the inlet to 8 mm at the outlet duct.

2.2. Gas phase

Isothermal simulations were performed using the commercial CFD package ANSYS FLUENT R14.0, which solves the Navier Stokes Equations using the finite volume method. Turbulence was modelled using the Stress-Omega Reynolds Stress Model (RSM) with shear flow corrections applied. Previous studies have determined RSMs to be the most capable RANS models for representing the flow topography in 3D diffuser flows [27,9]. Berdanier [8] compares the RSM Stress Omega formulation with other Reynolds Averaged Navier Stokes (RANS) models, noting that it gave the best representation of the recirculation region in a 2D diffuser. A full discussion on the use of RSM models in this case can be found in [26]. RSM models close the RANS equations by solving transport equations for the Reynolds stresses. The exact transport equations for the transport of the Reynolds stresses, $\rho\overline{u_i'u_j'}$, and the continuity and momentum equations are summarised in Table 1.

FLUENT's Enhanced Wall Function approach was used to represent the wall boundary layer, y^+ varied from 35 to 60 in the inlet pipe and from 5 to 50 in the diffuser and outlet duct due to the presence of the recirculation zone. The Enhanced Wall Function is formulated to extend from the viscous sub-region through the buffer layer to the log law layer by merging the two approaches [28]. Thus it gives a reasonable prediction in the buffer layer. This is of less concern here as ω based models, such as the Stress-Omega RSM used here, have been shown to improve the prediction of the buffer layer for favourable and adverse pressure gradients [29]. As the equations do not require the definition of viscous dampening coefficients, the ω equation can be reliably integrated throughout the boundary layer leading to a y^+ insensitive formulation. Concern regarding the wall treatment for separated flows is due to the prediction of the separation point of the boundary layer, k-ϵ models under-predict separation and k-ω models offer much improvement. Here this is of less concern as separation occurs at a defined point to the large divergent angle of the first expansion, which is analogous to a typically jet flow or backward facing step.

The pressure based solver with Pressure-Implicit with Splitting of Operators (PISO) algorithm was used for pressure correction [30]. This solves for mass conservation of the velocity field using a pressure equation. The PISO algorithm is part of the Semi-Implicit Method for Pressure-Linked Equations (SIMPLE) family, but PISO improves the efficiency by performing additional corrections for the fluxes after predicting the new velocity field from the pressure equation. This efficiency improvement makes it effective for transient problems. The convective and diffusion terms were represented using a second order upwind scheme. Time discretisation was achieved using the first order fully implicit scheme. The equation solver used was Algebraic Multigrid.

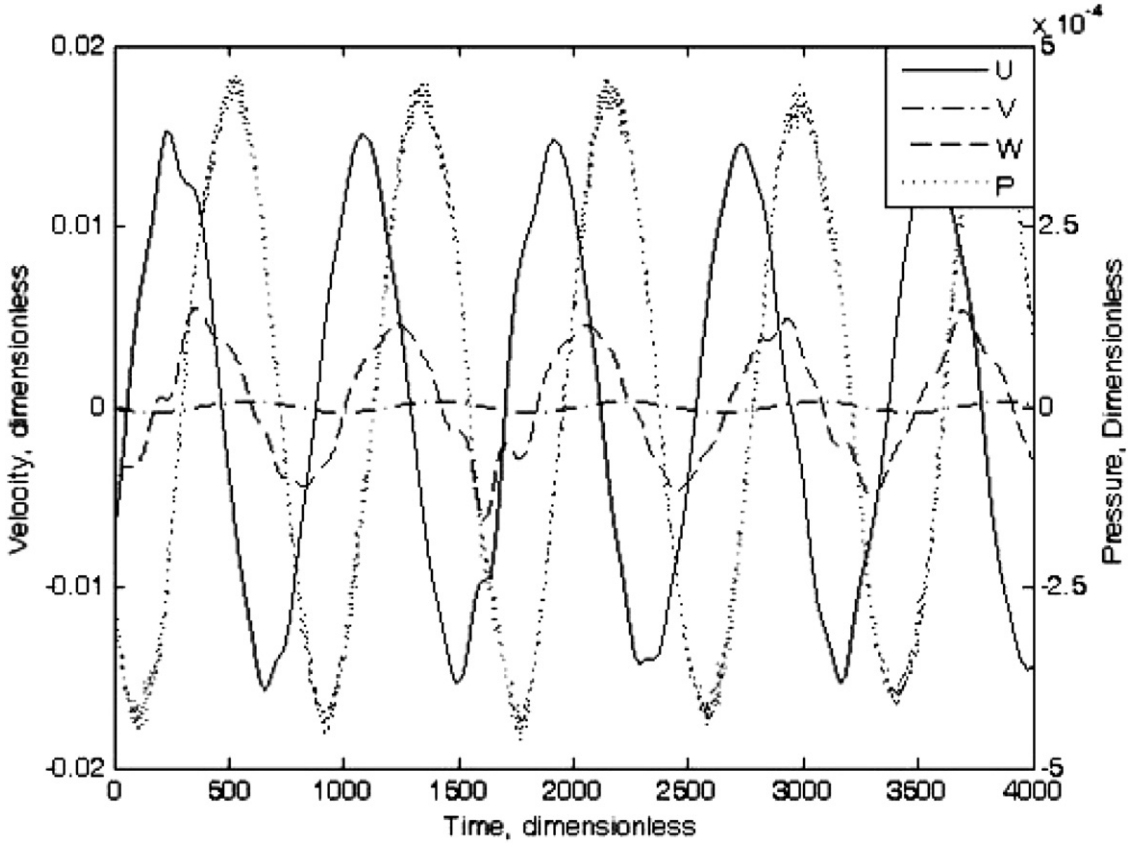

Fig. 4. Variation of the axial (V), secondary velocities (U, W) and pressure (P) with time.

Transient solutions were initialized from the steady state case, but the final solutions were independent of these initial solutions. The time step used was 2.5×10^{-4} s and further reduction in the time step did not significantly change the flow characteristics (Fig. 5). The Courant number typically ranged from 0.0003 to 0.5, except for the smallest cells at the diffuser inlet where it reached a value of 1.8 throughout the domain. The time-step analysis indicates that this did not affect the solution. Here the advancement of the coupled flow is limited by the continuous phase not the discrete phase. Gravity was defined in the negative y-direction as 9.81 m s^{-2}.

Convergence, for the air flow case, was judged based on the global sum of the residuals for the main flow variables and equations, which were allowed to approach the accuracy for single precision. The mass balance between the inlet and outlet of the domain was also monitored to ensure continuity. Finally, the velocity and pressure were monitored at various points until the frequency and magnitude of the oscillations did not change with further iteration. An example is shown in Fig. 4 for the variation of main flow variables with time. (Convergence for the particle phase was judged in the same way, however, the global sum of the residuals was judged to have converged for scaled values of 10^{-4} or less.) For each mass loading at least 2000 time steps (0.5 s) were simulated. After an initial settling period, no significant changes in the results were observed.

2.3. Discrete phase

The discrete phase was modelled as glass cenospheres ($\rho = 700$ kg m^{-3}). Results for two particle sizes, 10 and 60 μm ($St = 0.02$ and 0.78 respectively, based on upstream pipe flow), at various mass loadings of 0 to 1 $kg_{particles}/kg_{air}$ are presented. The particle phase was modelled using the Lagrangian approach with FLUENT's Discrete Particle Model. Here the Lagrangian tracking method is used to solve the individual trajectories of the theoretical particles by equating their inertia with external forces:

$$\frac{du_p}{dt} = F_D\left(u_p - u_g\right) + \frac{g\left(\rho_p - \rho_g\right)}{\rho_p}. \tag{2.1}$$

The second term on the right being the gravitational acceleration per unit mass. The drag force per unit mass, $F_D(\vec{u}_p - \vec{u}_c)$, is determined by the spherical drag law of Morsi and Alexander, for the drag coefficient:

$$F_D = \frac{3}{4}\frac{\mu_c Re_p}{\rho_p d_p^2} C_D \tag{2.2}$$

where Re_p is the particle Reynolds number,

$$Re_p = \frac{\rho_c d_p \left|\vec{u}_p - \vec{u}_c\right|}{\mu} \tag{2.3}$$

and C_D is defined

$$C_D = a_1 + \frac{a_2}{Re_p} + \frac{a_3}{Re_p^2} \tag{2.4}$$

for constants a_1, a_2 and a_3 [31]. Two-way coupling, for exchange of momentum between the particles and fluid, was accounted for. The magnitude of the Saffman lift force is typically at least one order of magnitude lower than the drag force for small particle sizes (≤100 μm) [32] and so it is not accounted for here. Due to the large density difference between the particles and the fluid the added mass force and basset force are insignificant in this case [33].

The average particle volume fractions are typically <0.001 [34] and so a particle collision model has not been included in this study. The recirculation zone results in local concentration of the particles and particle dispersion may be enhanced by treatment of particle–particle collisions at higher mass loadings.

The Discrete Random Walk (DRW) model has been used to model the effect of fluid turbulence on the particle path. The continuous phase velocity, $\vec{u}_c$ seen by the particle will be a combination of the averaged and fluctuating components due to turbulence, u_c'. The DRW models each component of this velocity using the following equation:

$$u_c', i = \zeta_i \sqrt{2k/3} \tag{2.5}$$

where k is the turbulent kinetic energy and ζ is a normally distributed random number [28]. Five random tries were defined for each inlet. In total 18,000 particle tracks were modelled. Whilst the continuous phase is modelled as time dependent, the particles have been treated as quasi-steady. In other words, the momentum source on the fluid due to the particles is updated per time-step. This particle treatment accounts for the effect of particle momentum on a standard steady-state fluid flow field whilst maintaining a transient solution for stability.

2.4. Boundary conditions

The inflow boundary condition was specified 25D upstream of the diffuser as a fully developed velocity profile parallel to the pipe axis. A characteristic length based on the inlet pipe diameter and an estimate

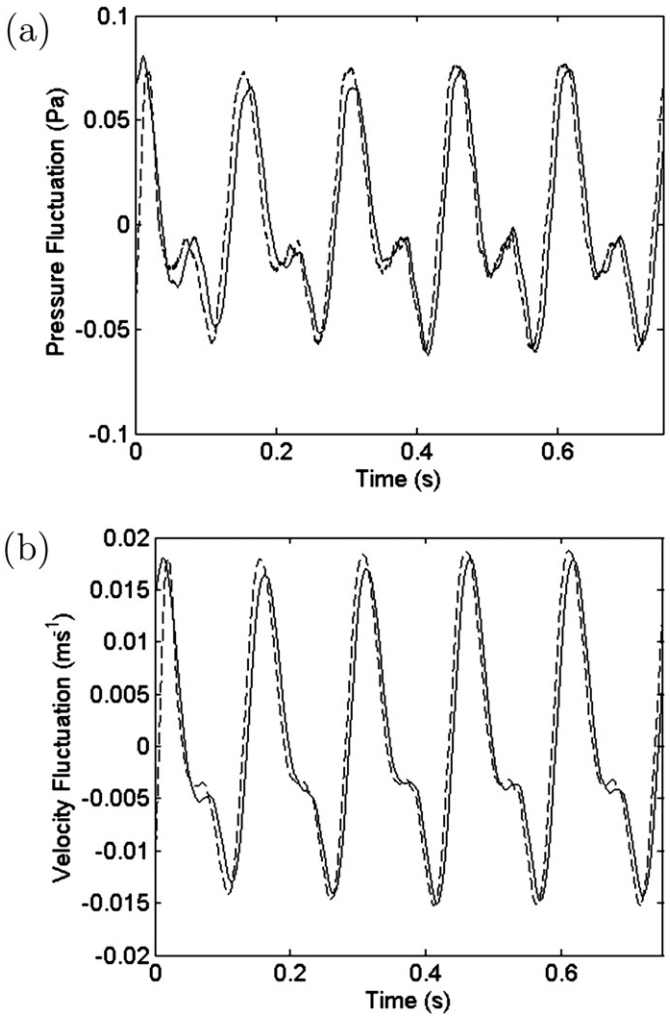

Fig. 5. Comparison of pressure and velocity fluctuations in the air flow only case with 0.15 ms [– – –] and 0.3 ms [—] time steps.

of turbulence intensity were also defined. The theoretical particle tracks were injected from the inlet surface with a velocity of 90% of the bulk velocity (14.4 m s^{-1}) and were suitably dispersed upon reaching the diffuser. A pressure outlet condition was used for the outflow. The outlet duct length of 40D was determined sufficient to not affect the flow at the diffuser. The reference pressure was set as atmospheric, where the pressure drop through the geometry was only 160 Pa.

On the wall surfaces a no slip boundary condition was defined for the fluid. Much work has been done on the interaction of particles with the wall [35,36] and whilst it is acknowledged that this is a function of wall roughness, impact angle and material properties, the particle wall interaction was modelled using a constant restitution coefficient of 0.9 in this study. This value is consistent for the interaction of glass particles with a smooth wall [35].

2.5. Initial conditions

The transient cases were initialized from the corresponding steady state case. It was observed that for both the steady state and transient cases the flow developed in the same way. The dispersed phase was injected into the fully converged air flow field. The mass loading of the discrete phase was ramped up slowly.

3. Results

3.1. Air flow field characteristics

A previous numerical investigation of the air flow case established the flow topography over a range of Reynolds numbers [26]. For *Re*

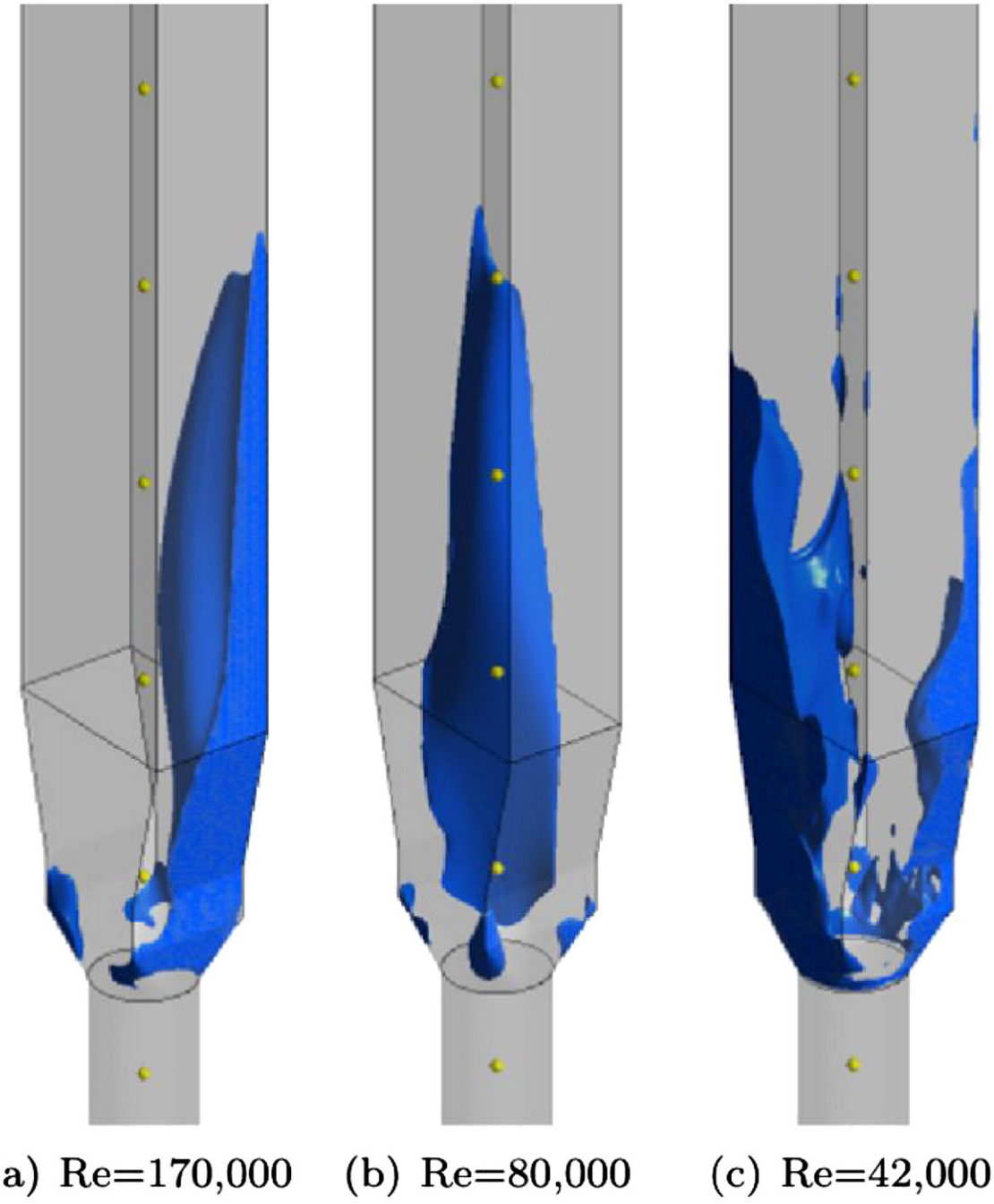

Fig. 6. Flow through the diffuser, showing the outline of the recirculation zone by isosurfaces for axial velocity of −0.01 m s^{-1}. The centreline monitor points — 1D, 1D, 3D, 5D, 7D and 9D are shown for reference.

> 80,000 one large recirculation became established within one corner of the diffuser (Fig. 6(a)). Upon reducing the flow rate, for $Re < 80{,}000$ greater separation took place, and the flow field was more chaotic (Fig. 6(c)). This transition has been attributed to the Coanda effect, or the jet's ability to entrain fluid at higher flow rates [37]. For a jet close to a wall the volume of fluid which can be entrained is limited, leading to the formation of a low pressure region and thus the jet deflects and becomes permanently attached to the wall. For a symmetrical 2D diffuser, Chiekh et al. [6] observed two stable states illustrating this phenomenon, where the flow was both deflected and attached to the top or the bottom wall. This formation of a lone recirculation zone in one corner is consistent with the circular-to-transition ducts of Miau et al. [3] and 2D and 3D diffuser geometries of Fox and Kline [5] and Steiner et al. [27].

This flow field is reasonably steady, and the only instability is a small scale precessing motion of the jet with characteristic frequency [26]. Fig. 3 shows a peak at 4.6 Hz for two different meshes. Consistent with the work of Fadai-Ghotbi et al. [38], who modelled a backward facing step flow on increasingly fine meshes with an unsteady RANS RSM approach, the high frequency instability of the shear layer reduced due to an associated decrease in numerical error. As will be described in the next section the resolution of large turbulent vortices in the shear layer is dependent on the particles, vortex shedding not being captured by the air flow field in this case as the random velocity fluctuations are filtered out by the RANS approach.

3.2. The effect of the discrete phase

The discrete phase was investigated for mono-dispersed particle sizes of 10 μm and 60 μm, over the mass loading range of 0.07 to 1 $kg_{particles}/kg_{air}$, and for an average air inlet velocity of 16 m s^{-1} ($Re = 170{,}000$). The importance of momentum coupling is assessed by comparing the drag force due to the dispersed phase with the momentum flux of the continuous phase. Crowe et al. [33] define the momentum coupling parameter as:

$$\Pi_{mom} = \frac{C}{St_{mom}}\left(1 - \frac{u_g}{u_p}\right) \tag{3.1}$$

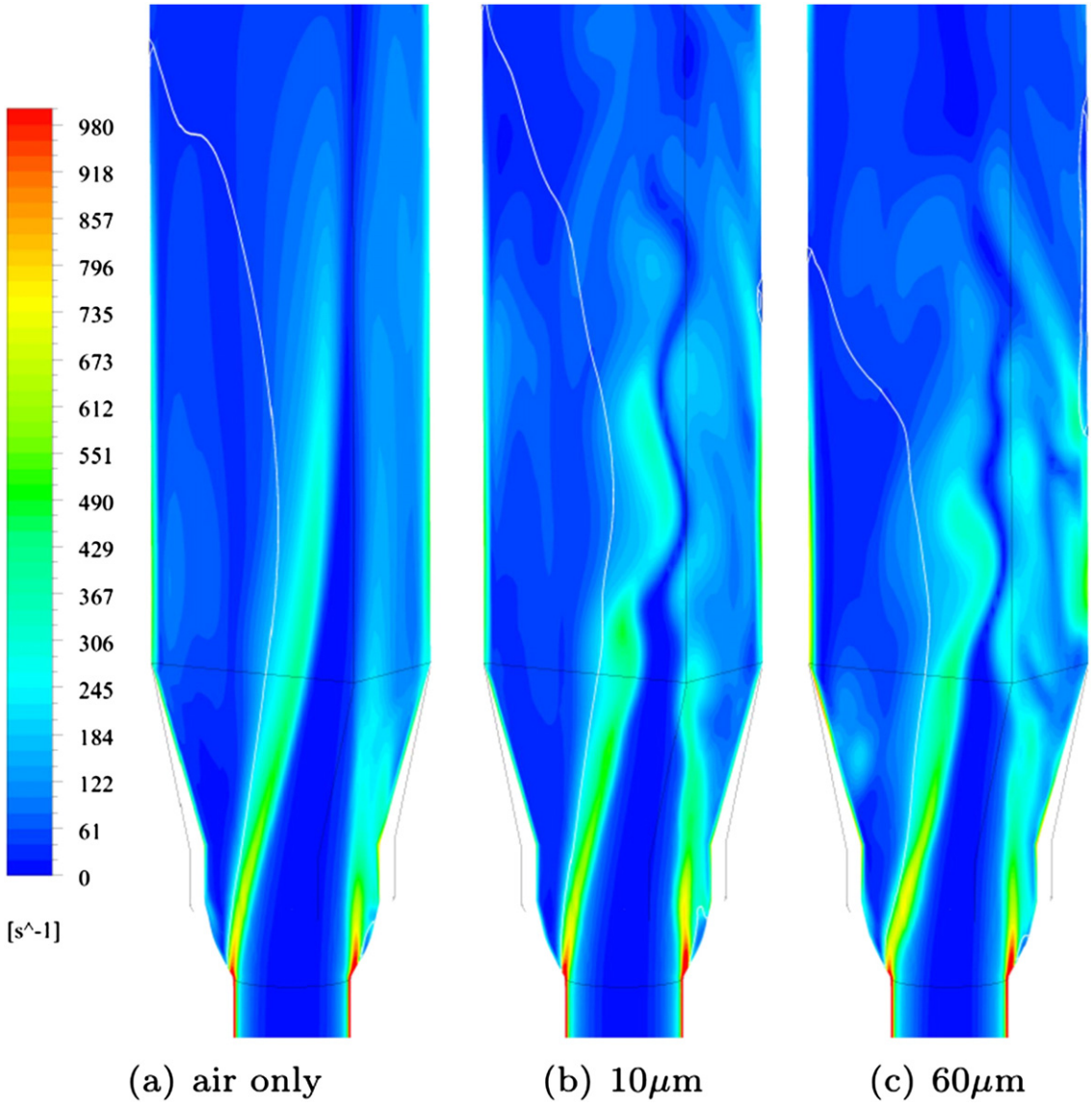

Fig. 7. Instantaneous vorticity contours (s^{-1}) showing an increase in vorticity at the leading edge of the recirculation zone for the 60 μm case ($Z = 0.07$ kg/kg). Recirculation zone outlined in white by contour of $V = -0.01$ m s^{-1}.

or as the Stokes number approaches 0,

$$\Pi_{mom} = \frac{C}{1 + St_{mom}} \tag{3.2}$$

where

$$St_{mom} = \frac{\tau_v u_g}{L} \tag{3.3}$$

is the momentum Stokes number. C is the dispersed phase concentration. u is the air velocity, and v is the particle velocity. τ_v is the particle response time, and L is the characteristic dimension of the system. A low value for this parameter would traditionally be associated with a one way coupled flow. In other words the discrete phase has little effect on the air flow field.

Table 2
Momentum coupling parameters for a mass loading of 0.07 $kg_{particles}/kg_{air}$.

Particle diameter (μm)	10	60
St_{mom} (expansion)	0.02	0.75
Π_{mom} ($U_{slip} = 0$ m s^{-1})	0.07	0.04
Π_{mom} ($U_{slip} = 2$ m s^{-1})	0.60	37.34

It was found that even for small mass loadings the discrete phase has a significant effect on the flow field. The introduction of the discrete phase has a number of effects: an increase in the relative density and momentum of the main jet and an inertial effect based on the particle Stokes number. This results in an increase in the vorticity generated at the leading edge of the main recirculation (Fig. 7), leading to the formation of coherent vortices in the shear layer which move downstream (Fig. 8). Furthermore, as few particles enter the recirculation zone it

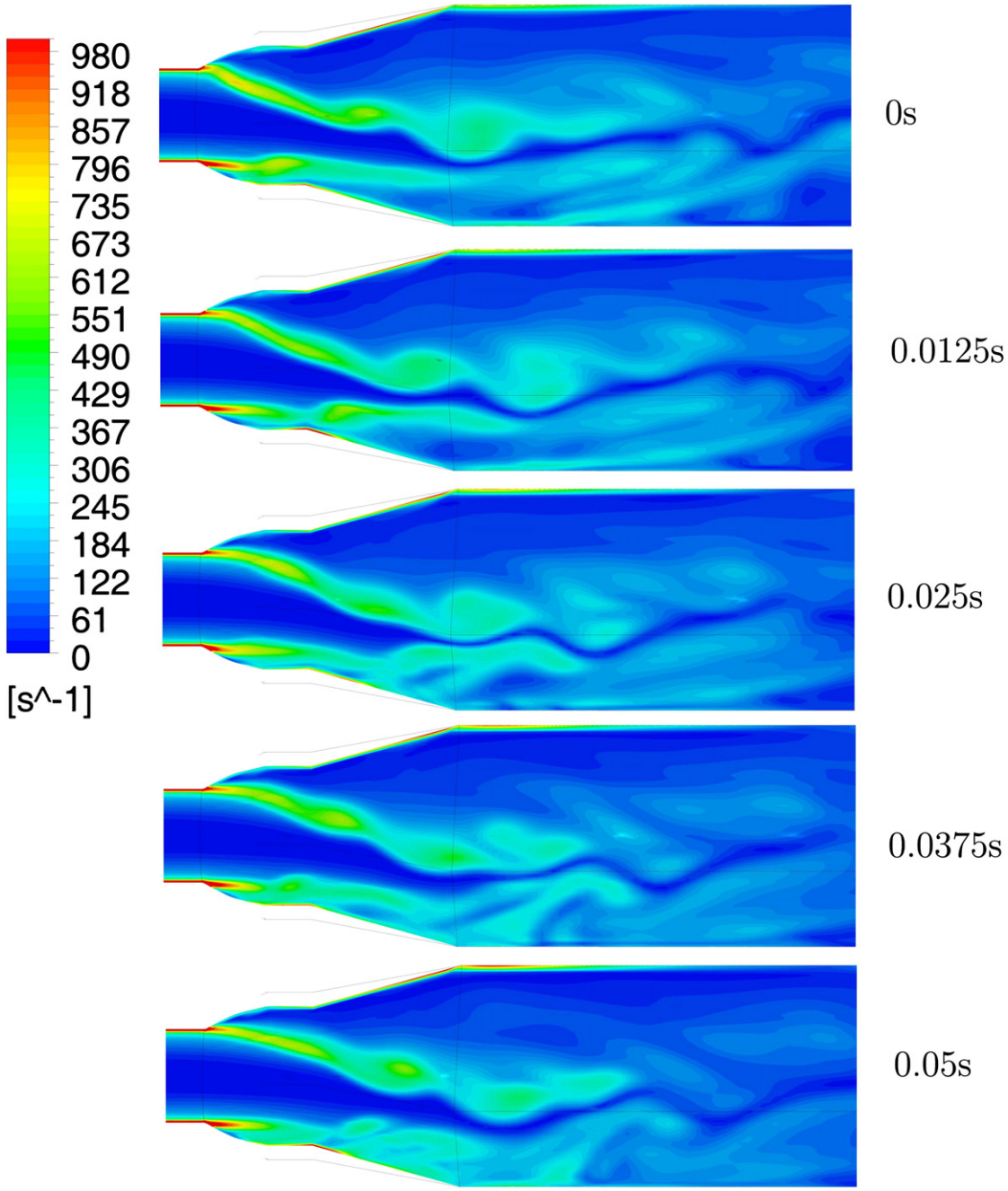

Fig. 8. Development of the vorticity field with time (60 μm particles and $Z = 0.07$).

will have a lower average density than the main jet, which will enhance this effect. Comparisons can be made to the Kelvin–Helmholtz instability in a density stratified shear layer [19].

Meiburg et al. [19] showed this effect in their numerical study, where the Kelvin–Helmholtz vortex showed motion in the direction of the seeded stream due to the generation of vorticity on this side. A mass loading of 0.5 was used in these cases and the vorticity magnitude is seen to increase substantially. In contrast, where both streams on either side of the shear layer were seeded equally with particles, the net effect was to redistribute the vorticity generation to the outside of the vortex with no net gain in vorticity generation. As shown in Fig. 7, the vorticity generation is highest at the leading edge of the recirculation in the 60 μm particle case. This leads to early formation of large vortices in the shear layer which entrain more of the surrounding fluid resulting in a decrease in the recirculation zone length. This effect is similar to periodic forcing to decrease or remove the stall region in diffuser flows which improves performance. The increase in vorticity is greatest for the 60 μm particles due to the greater inertia of these particles, which are not as easily deflected by the flow, and impact on the leading edge of the shear layer. The effect is captured here for the unsteady RANS modelling approach because the model is capable of generating distinct vortex structures upon application of a momentum source from the particles.

For such a low mass loading and low particle Stokes number it would be assumed that the effect of the discrete phase was insignificant and that momentum transfer between the phases could be ignored. However, in this case this assumption is not valid. The momentum coupling parameters for the 10 μm and 60 μm particles are shown in Table 2 for no slip velocity and a slip velocity of 2 m s^{-1}. Fig. 9 shows the variation in the particle slip velocity across the domain, with peaks

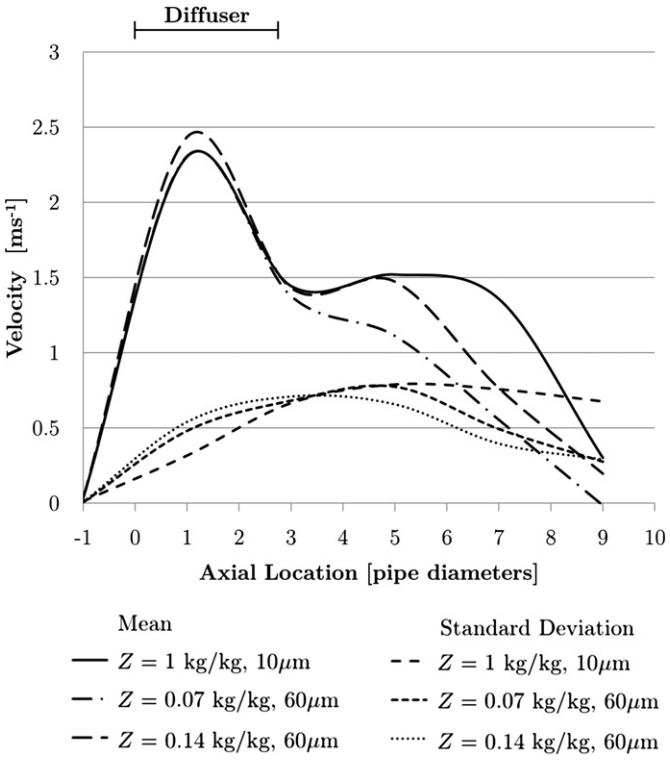

Fig. 10. Radial velocity and radial velocity fluctuation variation with axial location. Monitoring points were on the centreline at −1D, 1D, 3D, 5D, and 7D.

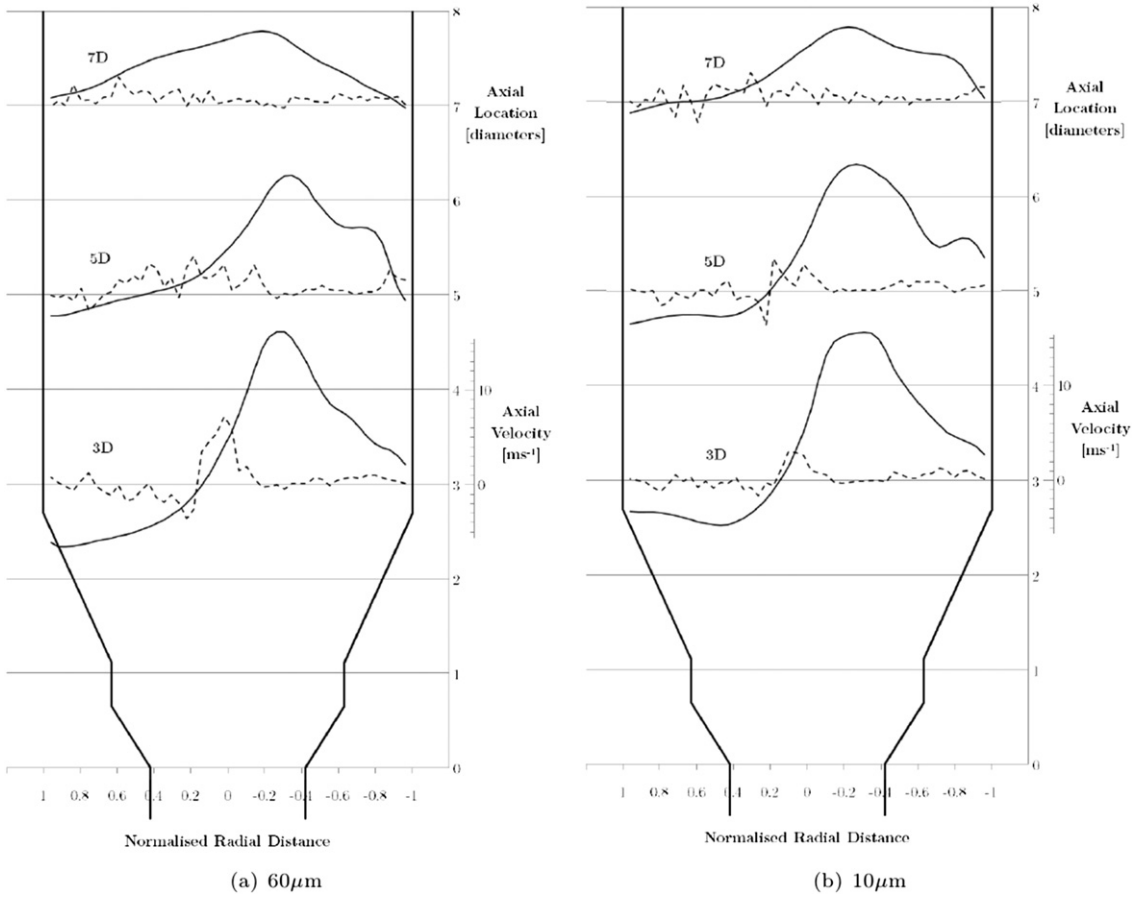

Fig. 9. Instantaneous profiles of air [—] and slip velocity [– – –] at axial distance of 3, 5 and 7D downstream of the diffuser entrance. The axial velocity is 0 m s^{-1} at each point on the axial location axis. Peaks in the slip velocity exist at the shear layer.

occurring near the shear layer. In the region of the shear layer the momentum coupling parameter can increase significantly due to the large magnitude of slip velocity between the phases. The particles do not slow down as quickly as the flow, and this results in a large transfer of momentum to the fluid when they do.

The significance of the momentum coupling for separated flows explains problems associated with obtaining adequately converged solutions for similar problems when treated as steady state. A steady state approach being a common simplifying assumption for such flows. This helps explain the instability initially seen in our bifurcator geometry.

3.3. The effect of mass loading

It has been shown that even for small mass loadings the discrete phase has an effect on the flow field. As the mass loading increases the model shows two effects taking place depending on the particle size.

Firstly, for the 10 μm particles with a Stokes number of 0.02, the flow field develops towards that of the 60 μm particle field at low mass loading (Figs. 11 and 12). As the mass loading of the discrete phase is increased the vorticity generated at the leading edge of the recirculation also increases. This leads to the large vortices first seen in the 60 μm case at a lower mass loading and an associated decrease in the length of the recirculation zone. Fig. 10 shows how the mean and standard deviation of the resultant velocity vary with mass loading and particle size. It can clearly be seen that the fluctuating velocity of the 10 μm particle case at a high mass loading approaches that of the 60 μm particle cases at low mass loading. In addition, the development of the largest turbulent fluctuations is delayed in the case of the 10 μm particles.

Founti and Kilpfel [20] found that the length of the recirculation zone after an axisymmetric sudden expansion in a diesel oil circuit initially decreased with increasing mass loading. The decrease in the recirculation zone length was attributed to an increase in the particle fluctuating velocity in the recirculation zone. Inter-particle collisions were responsible for lowering the particle fluctuating velocity and this was attributed to the subsequent increase in the recirculation zone length. However, the comparison of the model with and without inter-particle collisions shows only small differences. The authors attribute this to a limited number of tracked particles.

The 10 μm particle cases show an initial increase in the size of the recirculation zone with increasing mass loading, before the length decreases. This decrease can be attributed to an increase in vorticity magnitude. The role of inter-particle collisions has been neglected, although they may be responsible for an increase in the dispersion of the particles leading to an increase in the number being recirculated.

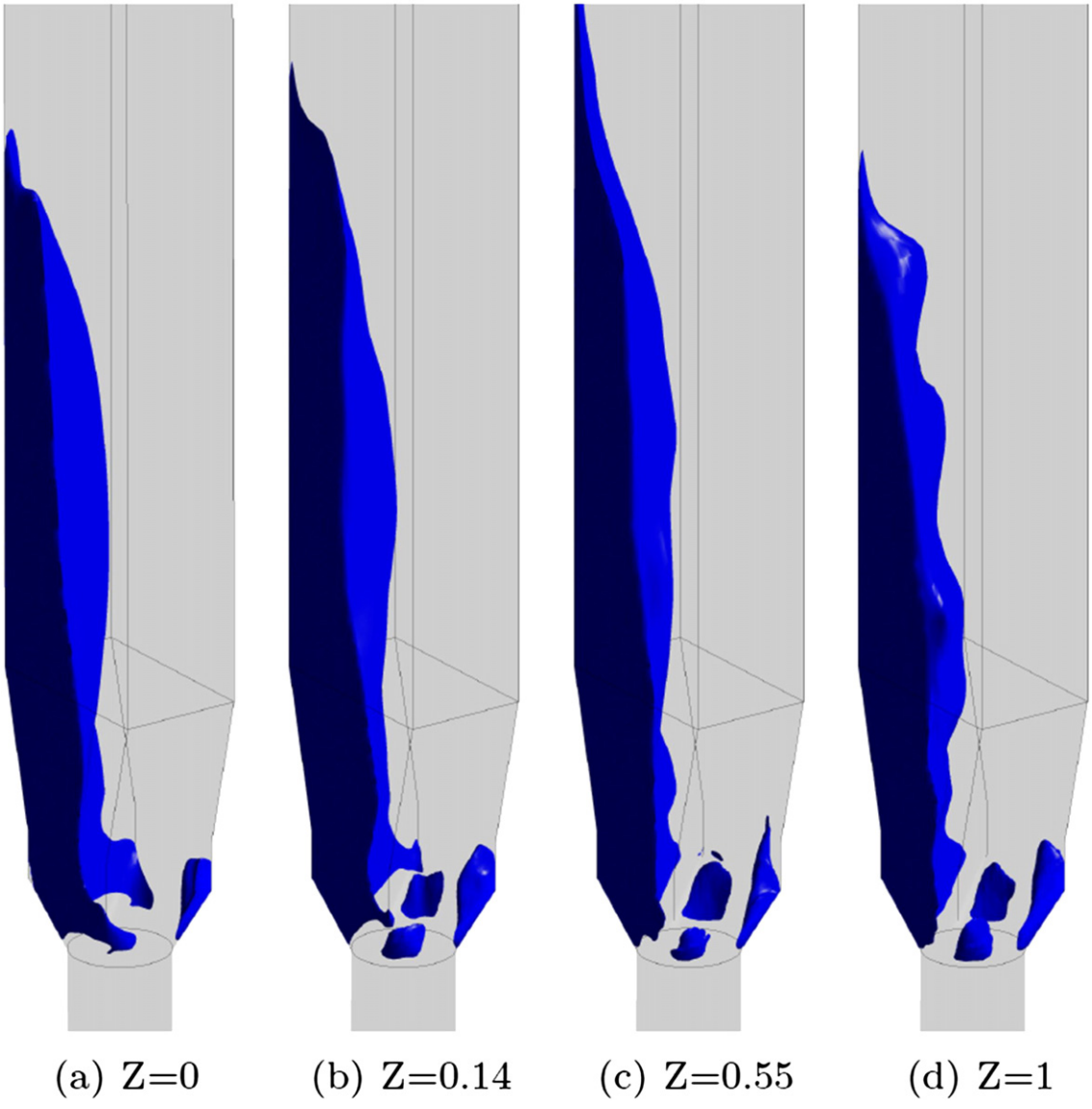

Fig. 11. Flow through the diffuser for $Re = 170{,}000$ and 10 μm particles, showing the outline of the recirculation zone by isosurfaces for axial velocity of -0.01 m s^{-1}.

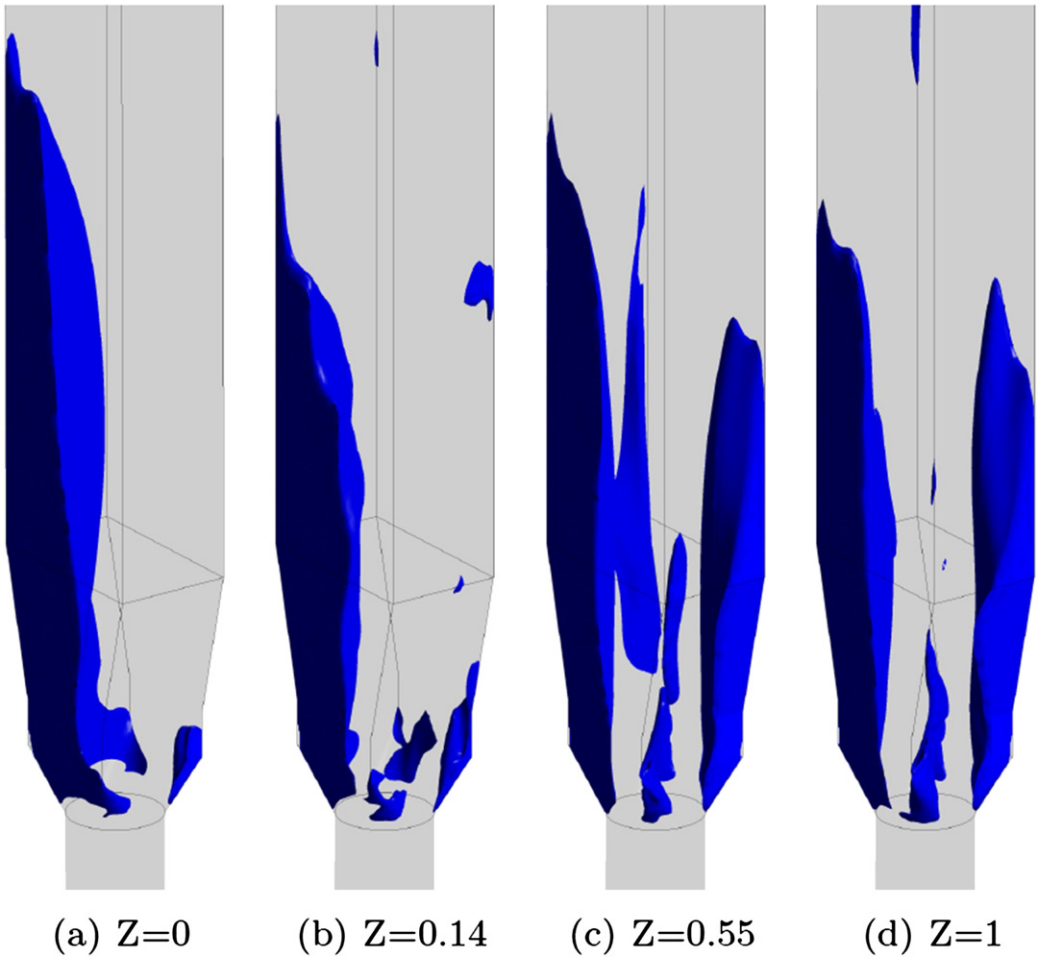

Fig. 12. Flow through the diffuser for $Re = 170{,}000$ and 60 μm particles, showing the outline of the recirculation zone by isosurfaces for axial velocity of -0.01 m s^{-1}.

So we are unable to test the hypothesis for the increase in the recirculation zone length of Founti and Kilpfel [20].

However, Hardalupas et al. [16] also found a lengthening of the recirculation zone with mass loading. This was attributed to the transfer of momentum from the discrete to the continuous phase. An increased dispersion of the particles in this case with mass loading was attributed to the modification of the gas phase turbulence, with an increase in mass loading resulting in large values for the RMS velocity of the gas phase. This agrees with our observation of an increase in the continuous phase turbulence with increasing mass loading (Fig. 10). In addition, as described above, a decrease in the recirculation zone length is associated with an increase in the size of the vortices.

It should also be noted from Fig. 10 that the deflection of the flow field within the diffuser propagates upstream into the inlet pipe up to 1D. This effect was also seen for the axisymmetric circular expansion featuring a precessing flow [7].

An increase in mass loading affects the flow field differently for the 60 μm particles with a Stokes number of 0.72. The flow field experiences a transition at a mass loading between 0.27 and 0.55 (Fig. 12). As the mass loading is increased the momentum of the jet also increases. Given the higher Stokes number of the particles, they are not as easily deflected by the recirculation when going through the expansion. Instead, they effectively increase the momentum of the jet causing greater separation and leading to the development of two large recirculation zones in opposing corners of the diffuser. Although the recirculation zone length is not increased beyond that of the air only case, the overall cross-sectional area of the recirculation zones is likely to have increased.

The attachment of the initial jet through the diffuser was attributed to the Coanda effect. The jet wants to entrain fluid, but in the vicinity of a wall the volume of fluid which can be entrained is limited. This leads to the generation of a low pressure region and the deflection of the jet towards the wall. The effect takes both time and a minimum flow rate to establish. The inclusion of the discrete phase increases the momentum of the jet and therefore the minimum flow rate at which the Coanda effect will establish itself has also increased.

It seems that the mechanism for the decrease in the recirculation zone length is due to the forcing effect from the particles on vortices in the shear layer. This effect is similar to periodic forcing to decrease or remove the separation in diffuser flows to improve performance as described by Garnier et al. [10]. This has the effect of increasing the size of the vortices leading to greater entrainment of the surrounding fluid and a decrease in the length of the recirculation zone. An increase in the length of the recirculation zone with mass loading has been noted by others and is likely to be due to an increase in the momentum of the main flow. A similar effect has been seen here for the 60 μm particle case. Therefore, this effect depends on the particle size and the geometry.

3.4. Recirculation of the particles

In order to enter the recirculation zone the particles must cross a dividing streamline. The particles are thus recirculated through interaction with the vortices.

Fig. 13 shows both contours of particle concentration and velocity vectors for a plane passing through the recirculation zone. The 10 μm particle case clearly shows that the particles concentrate between the

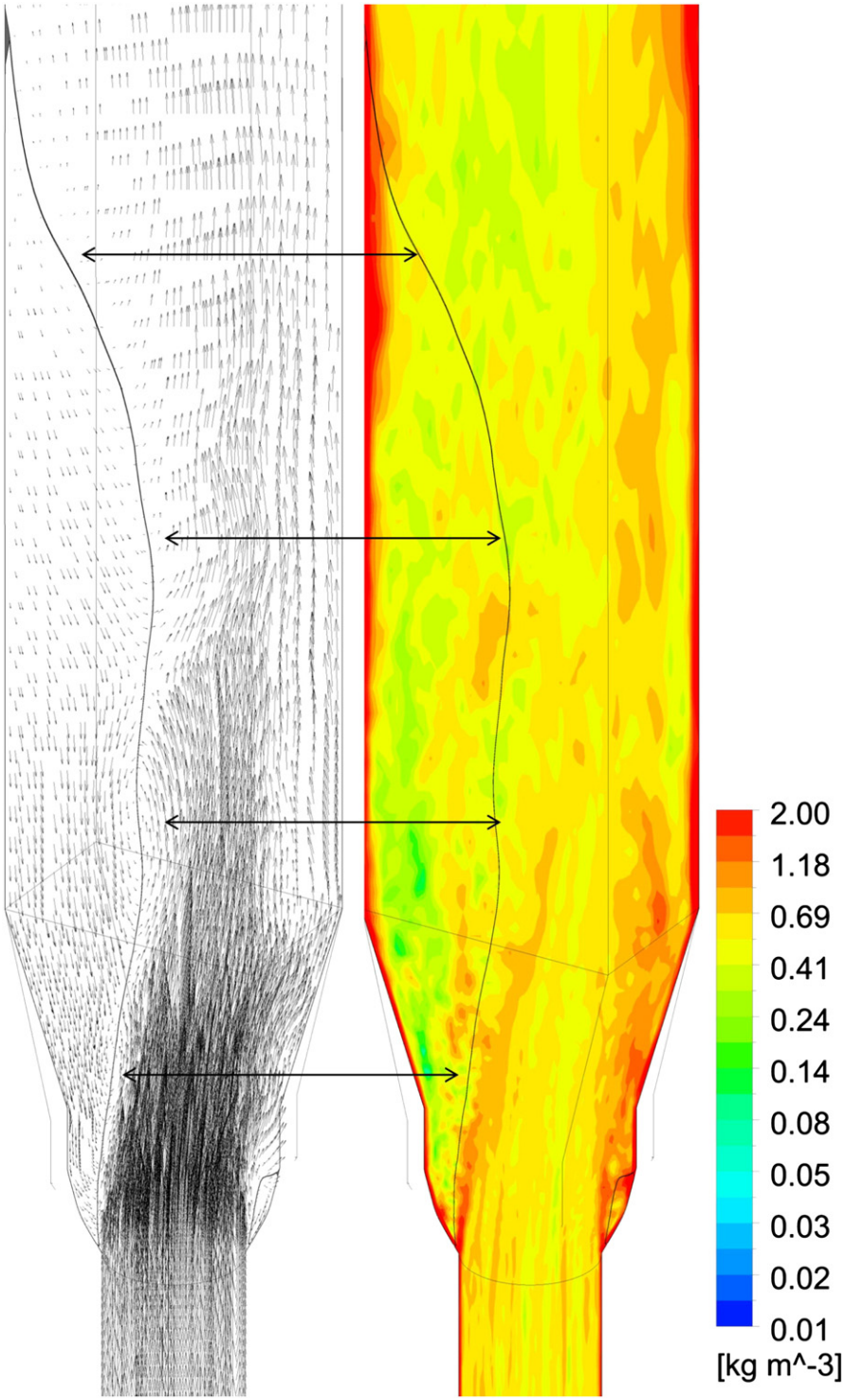

Fig. 13. Fluid velocity vectors (left) and contours of particle concentration (right) for a plane passing through the recirculation zone. The centre of the vortices, which correspond to regions of low particle concentration, are marked. The shear layer is shown by a black contour line.

vortex structures and are least concentrated at the centre of the vortices. Particles are recirculated as they are pulled off away from the main stream due to turbulent dispersion by the vortices. Eaton and Fessler [17] review the preferential concentration of particles in complex shear flows. It has been shown that particles concentrate in the highly strained region between vortex structures.

Table 3
Particle Stokes numbers.

Particle diameter (μm)	10	60
St_{pipe}	0.02	0.81
St_e ($U_{slip} = 0$ m s^{-1})	0.01	0.37
St_e ($U_{slip} = 2$ m s^{-1})	0.02	0.52

Hardalupas et al. [16] define a large eddy Stokes number as follows:

$$St_e = \frac{Re_h}{18}\frac{\rho_p}{\rho_g}\left(\frac{d_p}{h}\right)^2 \frac{U_0 + U_{slip}}{U_0} \tag{3.4}$$

where ρ_g and ρ_p are the densities of the fluid and particles, respectively, and d_p is the particle diameter. It is assumed that the length scale of the large eddies is the expansion step height, h, their convection velocity is the fluid average velocity and the corresponding Reynolds number of the fluid is based on the expansion step height.

Table 3 lists the Stokes numbers for both particle sizes, including the large eddy Stokes numbers for two slip velocities. All Stokes numbers are less than one and the large eddy Stokes numbers are less than the Stokes numbers of the particle in the upstream pipe. As a result the

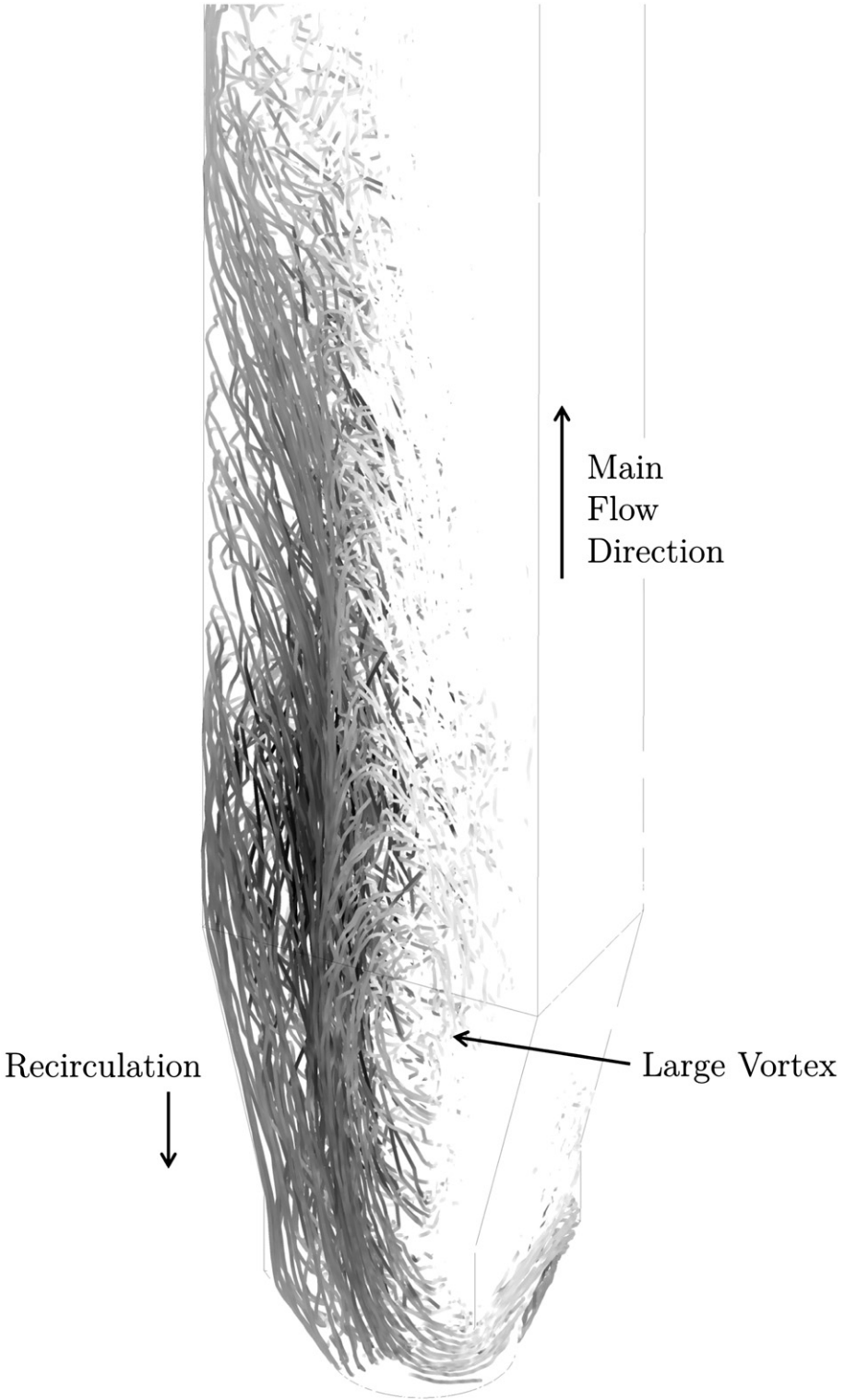

Fig. 14. Particle tracks, shaded for $v_p < 2$ m s^{-1}. The recirculation of the particles around the vortex near the exit of the diffuser can be seen.

particles are strongly affected by the vortices and thus recirculated. Hardalupas et al. [16] found a correlation between the large eddy Stokes number and the concentration of particles within the recirculation zone, with a sudden increase in the concentration occurring for a large eddy Stokes number of 1.

Therefore, the location the particles enter the recirculation zone depends on the location of the vortex. The vortex is shaped like a tube bent over the surface of the shear layer, thus the particles would be somewhat evenly recirculated across the surface of the shear layer where a vortex is present. However, the orientation of the vortex is altered by the asymmetric presence of the two walls. Fig. 14 attempts to show the particle tracks interacting with the recirculation zone. The vortices grow in size as they move downstream, and the velocity of the particles also decreases, therefore the large eddy Stokes number of the particles will continuously decrease as they traverse the recirculation zone. Thus a particle in the vicinity of the shear layer is more likely to be recirculated the closer it gets to the reattachment point. Due to the shape of the complex flow and the fact that a large vortex has become established by this point, the majority of particles are recirculated around the middle of the recirculation zone.

3.5. The effect of gravity

The effect of the direction of gravity was investigated for the 60 μm particle case and a mass loading of 0.14 kg/kg. This is a case where one large recirculation remains in one corner of the diffuser. Gravity was defined in the negative y direction, as previously described, and in the positive y direction. It was hypothesised that either the change in gravitational direction would cause more particles to be recirculated as they slowed down through the expansion and entered the recirculation under the effect of gravity, or with gravity in the positive y direction, more vorticity would be generated leading to larger vortices and greater recirculation of the particles.

Fig. 15 shows profiles of the particle concentration for the same diagonal profiles. Again gravity does not have a significant effect on the results. It can be seen that at 3D the concentration profile shows two peaks, one near the shear layer and the other at the centre of the main jet flow. Further downstream the majority of the particles are in the main jet flow. The low particle concentration at the center of the recirculation zone could be due to the recirculated particle trajectories being towards the walls, rather than corner, of the diffuser (as seen in Fig. 14).

The ratio of the drag force to the weight of the particles is calculated as:

$$\Phi = \frac{F_D\left(u_p - u_g\right)}{g}. \tag{3.5}$$

The small effect of gravity is because this ratio is >40 for a 60 μm particle, therefore the drag force dominates the particle trajectory in this flow. The recirculation of the particles is predominately due to the action of the large scale eddies.

4. Conclusions

The effect of particle flows on the air flow characteristics through a diffuser featuring a double expansion has been investigated using the commercial CFD code ANSYS FLUENT R14.0. Results for particles of 10 and 60 μm with mass loadings ranging from 0 to 1 kg/kg have been presented. The air flow field featured a large recirculation zone in one corner of the diffuser due to the Coanda effect. The flow field has been shown to be characterised by a small scale precessing motion of the jet previously [26].

The inclusion of the discrete phase caused an immediate change in the flow field. The discrete phase impacted on the shear layer, generating vorticity and leading to the movement of large, coherent vortices in the direction of the main flow stream. This effect occurred even at the smallest mass loadings, typically where such flows are assumed to be one way coupled. With an increase in mass loading or particle Stokes number the size of these vortices increased, leading to a reduction in the size of the recirculation as the vortices entrain more of the surrounding fluid. This is consistent with periodic forcing of the shear layer within diffusers to reduce the length of the recirculation.

For the case of the 60 μm particle as the mass loading increased the air flow field changed significantly. The increase in mass and the inertia of the particles gives the central jet greater momentum. As the presence of the lone recirculation zone is due to the Coanda effect, which takes both time and a minimum flow rate to establish, the increase in momentum reduces this effect. Two recirculations in opposing corners of the diffuser then develop.

In addition, the effect of reversing the direction of gravity has been investigated for the case of 60 μm particles. However, as the drag force is the dominant force governing the particle trajectory no discernible differences were observed.

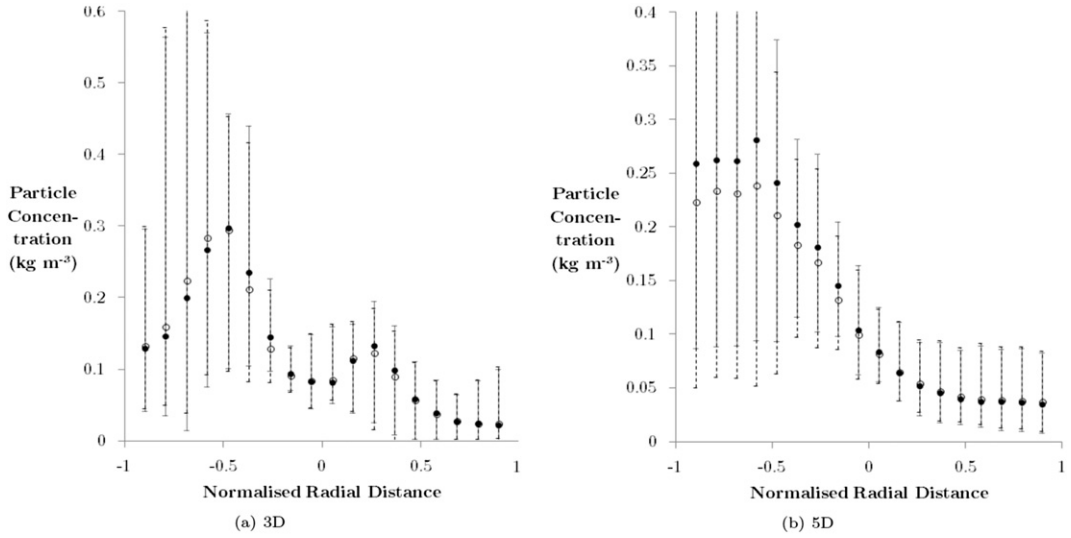

Fig. 15. Comparison of time averaged particle concentration profiles across the diffuser at 3D and 5D downstream of the diffuser entrance. • gravity acting against flow direction, ◦ gravity acting with flow direction. Vertical error bars show the variation in the results with time.

This work highlights the importance of using the correct approach when modelling gas–particle flows for industrial problems which often feature complex geometries and resulting flow fields. For flows which feature separation, such as expansions or diffusers, a RANS approach is likely to fail due to the possibility of instabilities in the flow field. Unsteady RANS is capable of capturing a number of effects as seen here upon addition of the discrete phase. It has been shown that the discrete phase can have a significant effect on the flow depending on both the particle size and mass loading. Of significance for numerical analysis is the limit of applicability of a steady state solver which is limited by not only particle–particle interactions, but also the interaction of the discrete phase with the air flow field.

Nomenclature

a	constant
C	discrete phase concentration, kg m^{-3}
C_D	spherical drag coefficient
d_p	particle diameter, m
D	pipe diameter, m
F_D	drag coefficient, s^{-1}
g	gravitational acceleration, m s^{-2}
h	expansion step height, m
k	turbulent kinetic energy, kg^{-1}
L	characteristic length, m
m_p	particle mass, kg
U_0	continuous phase velocity in expansion, m s^{-1}
U_{slip}	slip velocity, m s^{-1}
Re	Reynolds number
Re_h	Reynolds number based on expansion step height
St or St_{pipe}	Stokes number
St_{mom}	momentum Stokes number
St_e	large eddy Stokes number
t	time, s
u_c	continuous phase velocity, m s^{-1}
u_c'	continuous phase fluctuating velocity component, m s^{-1}
u_p	discrete phase velocity, m s^{-1}
v_p	discrete phase velocity in y-direction, m s^{-1}
Z	mass loading, $kg_{particles}/kg_{air}$
Π_{mom}	momentum coupling parameter
ρ_g	continuous phase density, kg m^{-3}
ρ_p	discrete phase density, kg m^{-3}
τ_v	particle response time, s
ζ_i	normally distributed random number

Acknowledgements

The authors gratefully acknowledge the support of Research Councils UK (RCUK), UK Engineering and Physical Sciences Research Council (EPSRC) (EP/G037345/1) and Doosan Power Systems Ltd.

References

[1] B. Kuan, W. Yang, Mal-distribution of coals in lignite-fired power station mill ducts: CFD simulations and experimental validation, International Conference on Coal Science and Technology, Okinawa, 2005, pp. 1–10.
[2] W.P. Patrick, D.C. Mccormick, Laser velocimeter and total pressure measurements in circular-to-rectangular transition ducts, Tech. Rep. 87, United Technologies Research Center, 1988.
[3] J.J. Miau, T.S. Leu, J.H. Chou, S.A. Lin, C. Lin, Flow distortion in a circular-to-rectangular transition duct, AIAA J. 28 (8) (1990) 1447–1456.
[4] D.O. Davis, F.B. Gessner, Experimental investigation of turbulent flow through a circular-to-rectangular transition duct, AIAA J. 30 (2) (1992) 367–375.
[5] R.W. Fox, S.J. Kline, Flow regimes in curved subsonic diffusers, J. Basic Eng. 84 (3) (1962) 303–312.
[6] M.B. Chiekh, J.-C. Bera, M. Sunyach, Synthetic jet control for flows in a diffuser: vectoring, spreading and mixing enhancement, J. Turbul. 4 (32) (2003) 37–41.
[7] B. Guo, T.A.G. Langrish, D.F. Fletcher, Numerical simulation of unsteady turbulent flow in axisymmetric sudden expansions, J. Fluids Eng. 123 (3) (2001) 574–587, http://dx.doi.org/10.1115/1.1374441 (URL http://link.aip.org/link/JFEGA4/v123/i3/p574/s1&Agg=do).
[8] R.A. Berdanier, Turbulent Flow Through an Asymmetric Plane Diffuser, Masters Purdue University, West Lafayette, Indiana, US, 2011.
[9] A. Karvinen, H. Ahlstedt, Comparison of turbulence models in case of three-dimensional diffuser, Proceedings of Open Source CFD International Conference 2008, No. 2008, 2008, pp. 1–17.
[10] E. Garnier, P. Pamart, J. Dandois, P. Sagaut, Evaluation of the unsteady RANS capabilities for separated flows control, Comput. Fluids 61 (2012) 39–45, http://dx.doi.org/10.1016/j.compfluid.2011.08.016 (URL http://linkinghub.elsevier.com/retrieve/pii/S0045793011002684).
[11] S. Lardeau, M. Leschziner, Unsteady RANS modelling of wake–blade interaction: computational requirements and limitations, Comput. Fluids 34 (1) (2005) 3–21, http://dx.doi.org/10.1016/j.compfluid.2004.04.001.
[12] G. Iaccarino, A. Ooi, P. Durbin, M. Behnia, Reynolds averaged simulation of unsteady separated flow, Int. J. Heat Fluid Flow 24 (2) (2003) 147–156, http://dx.doi.org/10.1016/S0142-727X(02)00210-2 (URL http://linkinghub.elsevier.com/retrieve/pii/S0142727X02002102).
[13] H. Schneider, D. von Terzi, H.-J. Bauer, W. Rodi, Reliable and accurate prediction of three-dimensional separation in asymmetric diffusers using large-eddy simulation, J. Fluids Eng. 132 (3) (2010) 031101, http://dx.doi.org/10.1115/1.4001009 (URL http://link.aip.org/link/JFEGA4/v132/i3/p031101/s1&Agg=doi).
[14] H. Schneider, D.A. Von Terzi, H.-J. Bauer, W. Rodi, A mechanism for control of turbulent separated flow in rectangular diffusers, J. Fluid Mech. 687 (2011) 584–594, http://dx.doi.org/10.1017/jfm.2011.395 (URL http://www.journals.cambridge.org/abstract_S0022112011003958).
[15] M. Chrigui, A. Sadiki, G.D. Ngoma, Unsteady turbulent two-phase flow using Euler/Lagrange approach devoted to two way coupling conditions, 7th International Conference on Multiphase Flow, 2010, pp. 1–7.
[16] Y. Hardalupas, A.M.K.P. Taylor, J.H. Whitelaw, Particle dispersion in a vertical round sudden-expansion flow, Philos. Trans. R. Soc. A Math. Phys. Eng. Sci. 341 (1662) (1992) 411–442, http://dx.doi.org/10.1098/rsta.1992.0110 (URL http://rsta.royalsocietypublishing.org/cgi/doi/10.1098/rsta.1992.0110).
[17] J.K. Eaton, J. Fessler, Preferential concentration of particle by turbulence, Int. J. Multiphase Flow 20 (1994) 169–209 (1).
[18] S. Horender, Y. Hardalupas, Turbulent particle mass flux in a two-phase shear flow, Powder Technol. 192 (2) (2009) 203–216, http://dx.doi.org/10.1016/j.powtec.2008.12.013 (URL http://linkinghub.elsevier.com/retrieve/pii/S0032591008005913).
[19] E. Meiburg, E. Wallner, A. Pagella, A. Riaz, C. Hartel, F. Necker, Vorticity dynamics of dilute two-way-coupled particle-laden mixing layers, J. Fluid Mech. 421 (2000) 185–227.
[20] M. Founti, A. Klipfel, Experimental and computational investigations of nearly dense two-phase sudden expansion flows, Exp. Thermal Fluid Sci. 17 (1998) 27–36.
[21] N. Huber, M. Sommerfeld, Modelling and numerical calculation of dilute-phase pneumatic conveying in pipe systems, Powder Technol. 99 (1) (1998) 90–101, http://dx.doi.org/10.1016/S0032-5910(98)00065-5 (URL http://linkinghub.elsevier.com/retrieve/pii/S0032591098000655).
[22] D. Giddings, a. Aroussi, S. Pickering, E. Mozaffari, A 1/4 scale test facility for PF transport in power station pipelines, Fuel 83 (16) (2004) 2195–2204, http://dx.doi.org/10.1016/j.fuel.2004.05.002 (URL http://linkinghub.elsevier.com/retrieve/pii/S0016236104001371).
[23] S. Laín, M. Sommerfeld, Characterisation of pneumatic conveying systems using the Euler/Lagrange approach, Powder Technol. 235 (2013) 764–782, http://dx.doi.org/10.1016/j.powtec.2012.11.029 (URL http://linkinghub.elsevier.com/retrieve/pii/S0032591012007784).
[24] J. Borée, T. Ishima, I. Flour, The effect of mass loading and inter-particle collisions on the development of the polydispersed two-phase flow downstream of a confined bluff body, J. Fluid Mech. 443 (2001) 129–165.
[25] M. Alletto, M. Breuer, One-way, two-way and four-way coupled LES predictions of a particle-laden turbulent flow at high mass loading downstream of a confined bluff body, Int. J. Multiphase Flow 45 (2012) 70–90.
[26] A. Love, D. Giddings, H. Power, Numerical Analysis of Vortex Dynamics in a Double Expansion, J. Fluids Eng. 135 (2013) 111104, http://dx.doi.org/10.1115/1.4024955.
[27] H. Steiner, S. Jakirlic, G. Kadavelil, R. Manceau, S. Saric, G. Brenn, 13th ERCOFTAC workshop on refined turbulence modelling, ERCOFTAC Bull. 78 (2008) 22–27.
[28] ANSYS Inc., ANSYS Academic Research, Release 14.0, ANSYS FLUENT user's guide, 2011.
[29] D. Wilcox, Comparison of two-equation turbulence models for boundary layers with pressure gradient, AIAA J. 31 (8) (1993) 1414–1421.
[30] R. Issa, Solution of the implicitly discretised fluid flow equations by operator-splitting, J. Comput. Phys. 62 (1986) 40–65.
[31] S.A. Morsi, A.J. Alexander, An investigation of particle trajectories in two-phase flow systems, J. Fluid Mech. 55 (1972) 193–208.
[32] J. Lataste, D. Huilier, H. Burnage, J. Bedna, On the shear lift force acting on heavy particles in a turbulent boundary layer, 34 (2000) 3963–3971.
[33] T.C. Crowe, J.D. Schwarzkopf, M. Sommerfeld, Y. Tsuji, Multiphase Flows with Droplets and Particles, second edition CRC Press, Taylor and Francis Group, 2012.
[34] S. Elghobashi, On predicting particle-laden turbulent flows, Appl. Sci. Res. 52 (1994) 309–329.
[35] M. Sommerfeld, N. Huber, Experimental analysis and modelling of particle–wall collisions, Int. J. Multiphase Flow 25 (6–7) (1999) 1457–1489, http://dx.doi.org/10.1016/S0301-9322(99)00047-6 (URL http://linkinghub.elsevier.com/retrieve/pii/S0301932299000476).

[36] B. Kuan, N. Rea, P. Schwarz, Application of CFD in the design of a grit collection system for the coal-fired power generation industry, Powder Technol. 179 (2007) 65–72.
[37] T. Panitz, D.T. Wasan, Flow attachment to solid surfaces: the Coanda effect, AICHE J. 18 (1) (1972) 51–57, http://dx.doi.org/10.1002/aic.690180111 (URL http://doi.wiley.com/10.1002/aic.690180111).
[38] A. Fadai-Ghotbi, R. Manceau, J. Borée, Revisiting URANS computations of the backward-facing step flow using second moment closures, Influ. Numer. Flow Turbul. Combust. 81 (3) (2008) 395–414, http://dx.doi.org/10.1007/s10494-008-9140-8 (URL http://link.springer.com/10.1007/s10494-008-9140-8).